ROYAL SOCIETY OF CHEMISTRY

Check for updates

Anisotropic Au nanobypyramids with molybdenum disulfide for plasmon-enhanced electrocatalysis, biosensing and energy production

Durgadas Datta,[ab] Ramakanta Mondal,[a] Ram Chandra Maji, [ID][b] Subin Yu,[cd] Dong-Il Won,[ce] Dong Ha Kim [ID]*[cefgh] and Swarup Kumar Maji [ID]*[a]

The strategic integration of anisotropic plasmonic nanostructures with two-dimensional (2D) semiconductors presents an emerging route for designing multifunctional hybrid systems with advanced photoelectrochemical (PEC) capabilities. In this work, we report the synthesis of a core–shell nanohybrid, Au nanobipyramid@MoS$_2$ (AuNBP@MoS$_2$), wherein gold nanobipyramids are uniformly encapsulated by few-layer MoS$_2$ nanosheets. This architecture promotes direct plasmon–semiconductor coupling under 808 nm near-infrared (NIR) excitation, enabling efficient hot electron generation, enhanced interfacial charge separation, and photothermal-assisted transport *via* localized surface plasmon resonance (LSPR). When immobilized on a glassy carbon electrode (AuNBP@MoS$_2$/GC), the hybrid device delivers exceptional PEC performance for both nonenzymatic biosensing and electrocatalysis. The sensor exhibits ultrasensitive detection of H$_2$O$_2$ and glucose with wide linear ranges (10 µM–30 mM and 100 µM–8 mM), low detection limits (7.25 µM and 5.95 µM), and high sensitivities (376.86 and 23.42 µA mM^{-1} cm^{-2}), accompanied by ∼11-fold photocurrent enhancement under LSPR. It further enables selective HeLa cancer cell detection *via* biomarker-triggered H$_2$O$_2$ release. In electrocatalysis, the hybrid electrode exhibits outstanding hydrogen evolution reaction (HER) activity, with a low onset potential (−0.18 V *vs.* RHE), an overpotential of −0.32 V at

[a] *Department of Chemistry, Khatra Adibasi Mahavidyalaya, Khatra 722140, West Bengal, India. E-mail: maji_swarup@yahoo.in*

[b] *Department of Chemistry, Bankura University, Bankura, West Bengal, India*

[c] *Department of Chemistry and Nanoscience, Division of Molecular and Life Sciences, College of Natural Sciences, Ewha Womans University, Seoul 03760, Republic of Korea. E-mail: dhkim@ewha.ac.kr*

[d] *Harvard Institute of Medicine, Harvard Medical School, Harvard University, Brigham and Women's Hospital, Boston, MA 02115, USA*

[e] *Nanobio Energy Materials Center (National Research Facilities and Equipment Center), Ewha Womans University, Seoul 03760, Republic of Korea*

[f] *College of Medicine, Ewha Womans University, 25, Magokdong-ro 2-gil, Gangseo-gu, Seoul 07804, Republic of Korea*

[g] *Graduate Program in Innovative Biomaterials Convergence, Ewha Womans University, 52 Ewhayeodae-gil, Seodaemun-gu, Seoul 03760, Republic of Korea*

[h] *Basic Sciences Research Institute (Priority Research Institute), Ewha Womans University, Seoul 03760, Republic of Korea*

New concepts

Biosensors for H$_2$O$_2$, glucose, and cancer cells are crucial for monitoring metabolic health, diagnosing diseases like diabetes, and enabling early and selective detection of cancer biomarkers, respectively. The advantage of developing a new type of hybrid material, such as the AuNBP@MoS$_2$ nanohybrid, lies in its direct plasmon-enhanced dual-mode biosensing property and HER activity. This unique architecture facilitates efficient hot electron generation, enhanced interfacial charge separation, and photothermal-assisted transport under NIR excitation, leading to an exceptional level of photoelectrochemical performance. For the first time, we investigate the dual-mode biosensing capabilities of this platform, enabling ultrasensitive, high-sensitivity detection of H$_2$O$_2$ or glucose and selective cancer cell detection, alongside its outstanding hydrogen evolution reaction activity, showcasing a powerful synergistic platform for both advanced biosensing and sustainable energy applications.

10 mA cm^{-2}, and a Tafel slope of 92 mV dec^{-1} under NIR illumination. Addition of ethanol as a sacrificial agent further reduces the overpotential to −0.316 V and enhances the exchange current density by ∼12-fold due to suppressed charge recombination and improved hot carrier utilization. Mechanistic investigations combining experimental and theoretical analyses attribute these enhancements to synergistic plasmonic effects, efficient hot electron injection, and photothermal contributions. This work underscores the immense potential of anisotropic plasmonic–semiconductor hybrids in driving next-generation technologies for biosensing, electrocatalysis, and sustainable energy applications.

Introduction

The advancement of high-performance biosensors remains a critical pursuit across biomedical diagnostics, environmental surveillance, and industrial process monitoring. Among various analytes of physiological and pathological relevance, hydrogen peroxide (H$_2$O$_2$) occupies a pivotal position owing to its dual role as a cellular messenger and a hallmark of oxidative stress.[1,2] As a key reactive oxygen species (ROS), H$_2$O$_2$ is

generated *in vivo* through enzymatic and non-enzymatic oxidative processes and participates in diverse biochemical pathways involving glucose oxidase, cholesterol oxidase, amino acid oxidases, and mitochondrial respiration.[3] While physiologically regulated concentrations of H_2O_2 are crucial for maintaining redox homeostasis and signal transduction, aberrant levels are directly linked to the onset and progression of several degenerative and inflammatory diseases including atherosclerosis, myocardial infarction, neurodegenerative disorders (*e.g.*, Parkinson's and Alzheimer's), and multiple forms of cancer.[4] Therefore, the precise, real-time, and *in situ* detection of H_2O_2 is indispensable for both fundamental biological research and early clinical diagnostics.[5,6] Beyond its direct biomedical significance, H_2O_2 also serves as a quantitative reporter molecule in enzymatic biosensing, particularly in glucose detection, where its production *via* glucose oxidase-catalysed oxidation is stoichiometrically correlated with glucose concentration.[7] Such enzyme-based electrochemical biosensors constitute the gold standard for diabetes monitoring.[8] Furthermore, recent advances in redox biology have underscored the relevance of H_2O_2 as a biomarker for cancer cell detection, given that cancer cells exhibit elevated ROS production due to aberrant metabolism and mitochondrial dysfunction.[9] In this context, the indirect electrochemical sensing of H_2O_2 released by live cancer cells has emerged as a powerful approach for non-invasive cancer diagnosis.[5,10] Electrochemical biosensors, in particular, have garnered widespread attention due to their high sensitivity, rapid response, miniaturization capability, operational simplicity, and cost-effectiveness.[3] Integrating nanomaterials with redox-active surfaces enhances electron transfer kinetics, increases analyte binding affinity, and improves overall signal-to-noise ratios, making them promising candidates for next-generation biosensing platforms.[11]

Concurrently, the escalating demand for sustainable energy solutions has catalysed extensive research into hydrogen (H_2) production *via* water electrolysis, with the hydrogen evolution reaction (HER) at the cathode playing a central role.[12] Molecular hydrogen is a clean, high-energy-density fuel whose combustion yields only water, positioning it as a cornerstone of future energy infrastructures.[13] However, the widespread adoption of electrochemical H_2 production remains hindered by the reliance on scarce and costly noble metal catalysts such as platinum (Pt), rhodium (Rh), and palladium (Pd).[14] This has driven the search for earth-abundant, low-cost, and efficient HER electrocatalysts. Among emerging materials, two-dimensional (2D) transition metal dichalcogenides (TMDs), especially molybdenum disulfide (MoS_2), have gained significant traction due to their layered structure and tunable electronic properties and exposure of catalytically active edge sites.[15] Since semiconducting 2H-MoS_2 suffers from low electrical conductivity, strategies such as phase transformation to metallic 1T-MoS_2 and hybridization with conductive substrates or nanostructures have been employed to overcome this limitation.[16,17]

An emerging strategy to boost the performance of such systems involves coupling TMDs with plasmonic nanostructures. Noble metals such as gold (Au), silver (Ag), and copper (Cu) exhibit localized surface plasmon resonance (LSPR), a collective oscillation of conduction electrons under resonant light excitation, resulting in the generation of energetic hot carriers and enhanced local electromagnetic fields.[18–20] These plasmonic effects can be harnessed to promote photothermal heating, increase surface reaction rates, and drive charge transfer processes across metal–semiconductor interfaces.[21] When coupled with semiconductors, hot electrons from plasmonic metals can be injected into the conduction band of the adjacent semiconductor, effectively enhancing photocatalytic or electrocatalytic activity by promoting charge separation and minimizing recombination losses.[18–22] Notably, anisotropic plasmonic nanostructures (AuNSs) offer further advantages due to their shape-dependent optical properties.[19] Their sharp tips support strong LSPR in both visible and near-infrared (NIR) regions and localize intense electromagnetic fields ("hot spots"), which amplify hot electron generation and enhance sensitivity in light-assisted applications.[18–26]

In this context, the mechanistic understanding of plasmon-induced hot electron injection into semiconductors has greatly advanced our knowledge of light–matter interactions at the nanoscale. Initially demonstrated in the early 2000s, this phenomenon enables energetic electrons, generated *via* LSPR, to transfer across metal–semiconductor interfaces and drive redox reactions.[27] A key breakthrough came in 2015 when Xia *et al.* introduced the concept of direct plasmon-accelerated electrochemical reactions (PAER), reporting an $\sim$3-fold HER enhancement using an Au–MoS_2 hybrid under NIR-light excitation.[18] Since then, a range of plasmonic–semiconductor nanostructures, such as winged Au@MoS_2,[28] core–shell Au–MoS_2,[29] AuNP@rGO@Pd,[30] and AgAuNPs/Co-MOFNs,[31] have demonstrated improved HER activity due to enhanced light harvesting, hot carrier transfer, and local photothermal effects. Similarly, PAER-active nanostructures have been used for photoelectrochemical (PEC) biosensing of analytes including H_2O_2, glucose, ascorbic acid, and cancer cells, with platforms

Dong Ha Kim

Celebrating a decade of significant contributions to nanoscale science, Nanoscale Horizons has established itself as a premier platform for advancing nanotechnology. Since joining the Advisory Board in March 2019, I have been privileged to support the journal's mission and to contribute to this special issue through our work on multifunctional anisotropic plasmonic nanomaterials. Over the past decade, the journal has highlighted innovations shaping the future of the field. Looking forward, I am confident it will remain a central venue for driving innovation and fostering impactful discoveries in nanoscience and nanotechnology.
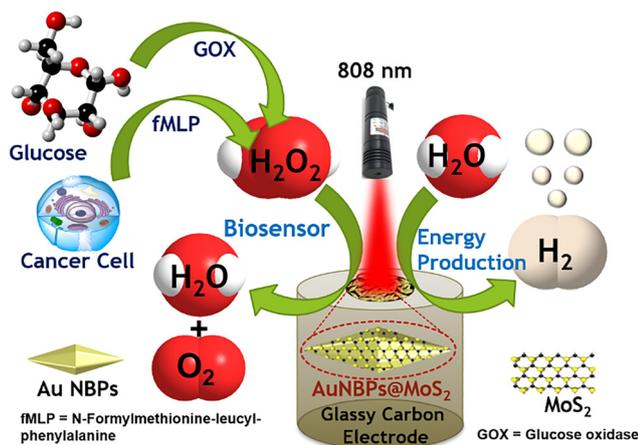
Scheme 1 Schematic representation of the enhanced electrochemical performances of AuNBPs@MoS$_2$ upon LSPR excitation.

like AuAg@rGO,[32] PTA nanobipyramids,[33] and our previously developed AuNRs[34] and AuNRs@rGO[35] exhibiting significant LSPR-driven signal enhancement. Despite this progress, the field still lacks a comprehensive mechanistic framework. Issues such as carrier lifetime, interfacial energetics, and structure–activity relationships remain unresolved. Therefore, further development of efficient, robust PAER platforms, coupled with in-depth mechanistic investigations, is essential to translate this emerging strategy into real-world applications in energy conversion and biomedical diagnostics (Scheme 1).

In this work, we present a rationally designed core–shell hybrid nanostructure composed of gold nanobipyramids wrapped with few-layer MoS$_2$ nanosheets (AuNBP@MoS$_2$). The AuNBPs were surface-functionalized with 3-amino-propyltriethoxysilane (APTES) to facilitate electrostatic interaction and uniform wrapping with exfoliated ce-MoS$_2$. The resulting hybrid was integrated onto a glassy carbon (GC) electrode to fabricate a multifunctional PEC platform, capable of dual channel non-enzymatic, ultrasensitive detection of H$_2$O$_2$, glucose, and cancer cells, as well as facilitating efficient plasmon-assisted hydrogen evolution. Under 808 nm NIR LSPR excitation, the system exhibited enhanced photocurrent response, superior charge separation dynamics, and prolonged hot carrier lifetimes. Furthermore, in the presence of ethanol as a hole scavenger, the hybrid displayed significantly improved HER activity, demonstrating its dual capability for biosensing and sustainable energy generation. This work highlights the synergistic coupling of plasmonic and catalytic functionalities within a single nanostructure, paving the way for development of advanced multifunctional materials for diagnostics and green energy technologies.

Experimental

Chemicals

The following high-purity chemicals were procured from Sigma-Aldrich and used without further purification: gold(III) chloride trihydrate (HAuCl$_4$·3H$_2$O, $\geq$99.9%), sodium borohydride (NaBH$_4$, 99%), trisodium citrate dihydrate, and *N*-formylmethionyl-leucyl-phenylalanine (fMLP), silver nitrate (AgNO$_3$, $\geq$99%), L-ascorbic acid, cetyltrimethylammonium bromide (CTAB, $\geq$98%), cetyltrimethylammonium chloride (CTAC, $\geq$98%), (3-aminopropyl)triethoxysilane (APTES, 99%), phosphate-buffered saline (PBS) tablets, concentrated hydrochloric acid (HCl, 37%), molybdenum disulfide powder (MoS$_2$, 99%), *n*-butyllithium solution, Nafion perfluorinated resin, and glucose oxidase (GOx). Aqueous hydrogen peroxide solution (H$_2$O$_2$, 30%) was sourced from Finar Limited and ammonium hydroxide (NH$_4$OH, 30%) was acquired from Merck.

Synthesis of AuNBPs@MoS$_2$ NPs

AuNBPs and MoS$_2$ NSs were prepared by the previously reported methods of Wang *et al.* and Chou *et al.*, respectively.[36,37] Then, a 2 mL aqueous solution of Au NBPs and 50 μL of APTES were mixed and stirred for 30 min. The amine functionalized AuNBPs were collected by centrifugation at 8000 rpm for 10 min and again redispersed in 2 mL of water. The obtained AuNBP solution was then added to 5 mL aqueous solution of chemically exfoliated MoS$_2$ (3.0×10^{-7} M) dropwise under vortexing. The reaction was continued for 24 h under very slow stirring and AuNBP@MoS$_2$ was collected by centrifugation and purified by washing with water two times.

Electrochemical measurements

Electrochemical measurements were performed using a conventional three-electrode configuration, comprising a platinum wire counter electrode, an Ag/AgCl reference electrode, and a glassy carbon working electrode functionalized with AuNBP@-MoS$_2$ nanocomposites (AuNBP@MoS$_2$/GC). The working electrode was prepared *via* drop-casting: 4 mL of the synthesized AuNBP@MoS$_2$ dispersion was centrifuged, and the resulting precipitate was redispersed in a 50 μL ethanolic solution containing 0.5% Nafion (5 μL). Subsequently, 4 μL of this homogeneous suspension was deposited onto the GC electrode surface (3 mm diameter) and allowed to dry under ambient conditions. PEC biosensing studies for H$_2$O$_2$ and glucose were conducted in 25 mL of 0.1 M PBS (pH 7.4) at 25 °C. HER performance was evaluated in 0.5 M H$_2$SO$_4$ electrolyte at room temperature (25 °C). For cancer cell detection, electrochemical measurements were performed in 10 mL of PBS (0.1 M, pH 7.4) containing a cellular suspension with a density of approximately 9.0×10^9 cells per mL.

Instruments and measurements

Microstructural characterization was performed using field emission scanning electron microscopy (FESEM, JEOL JSM6700-F) and high-resolution transmission electron microscopy (HR-TEM, JEOL JSM2100-F operated at 100 kV). Optical properties were analyzed through UV-vis-NIR spectroscopy (Varian Cary5000 spectrophotometer) and Raman spectroscopy (LabRam HREvo 800 system, HORIBA Jobin Yvon). Electrochemical measurements were carried out using a CH Instruments 600SE potentiostat/galvanostat system. For photoelectrochemical

studies, an 808 nm near-infrared laser (IRM808TA-3000FC, SLOC Co. Ltd) served as the excitation source. Cellular imaging was conducted using a Nikon D-Eclipse C1 confocal fluorescence microscope.

Finite-difference time-domain (FDTD) simulation studies

Optical simulations were performed using Lumerical FDTD Solutions to calculate electric field distribution. An 808 nm plane wave source excited single Au NBPs, with periodic boundaries along the x- and y-axes and a PML along the z-axis. The mesh size was set to 0.5 nm, and the surrounding medium was modeled as water ($n = 1.33$). Optical constants for Au and MoS_2 were taken from Johnson and Christy and the previous literature, respectively.[38,39] The sizes of Au NBPs and AuNBP@MoS_2 were based on TEM-derived averages.

Results and discussion

Synthesis and characterization of AuNBPs@MoS_2 NPs

Monodisperse AuNBPs and 2D MoS_2 NSs were synthesized following the reported procedures by Wang *et al.* and Chou *et al.*, respectively.[36,37] The 2D MoS_2 NSs were obtained *via* lithium ion-intercalation and subsequent chemical exfoliation of bulk MoS_2. Meanwhile, the Au NBPs were produced through a seed-mediated growth approach and later modified with APTES to enhance electrostatic binding. The corresponding FESEM and TEM images of AuNBPs and MoS_2 NSs are provided in Fig. S1. The AuNBPs exhibited a highly uniform bipyramidal morphology with an average length of 110 nm and a width of 35 nm having the aspect ratio of 3.14. Hybrid core@shell nanostructures (AuNBP@MoS_2) were subsequently prepared by uniform encapsulation of AuNBPs with MoS_2 NSs using an electrostatic interaction mechanism by a modified version of

our previously reported protocol.[37] The resulting hybrid material showed a well-defined wrapping of AuNBPs by ~ 5 nm thicker 2D MoS_2 NSs, as observed in Fig. 1a–c. HRTEM analysis (Fig. 1d) revealed the highly crystalline nature of the AuNBPs, characterized by sharp vertices and well-defined facets. A lattice spacing of 2.34 Å corresponding to the (111) crystal plane of Au was observed. The consistent morphology and size distribution indicate a well-controlled synthesis with minimal aggregation, ensuring high reproducibility. Zeta potential measurements (Fig. 1e) confirmed the stepwise surface modification during hybrid formation. The surface charge shifted from +14.6 mV (for AuNBPs) to −11.3 mV after MoS_2 coating, indicating successful deposition of negatively charged MoS_2 NSs onto the AuNBP surface. Energy-dispersive X-ray spectroscopy (EDS) analysis (Fig. 1f) displayed distinct elemental peaks corresponding to Au (2.1, 9.7, and 11.4 keV), Mo (2.3, 17.4, and 19.6 keV), and S (~ 2.3 keV), confirming the presence of both AuNBPs and MoS_2 in the hybrid nanostructure.[37] Raman spectroscopy (Fig. 1g) further validated the presence of MoS_2 through its characteristic vibrational modes, E_{2g} and A_{1g}, observed at 378.4 and 407.9 cm^{-1}, respectively.[18] Upon integration with AuNBPs, a slight blueshift (~ 2 cm^{-1}) and an enhancement in Raman intensity were noted, attributed to strong interfacial interactions and the surface-enhanced Raman scattering (SERS) effect induced by AuNBPs, which well matched with previous reports.[40] Optical properties were examined by UV-vis-NIR absorption spectroscopy (Fig. 1f). The characteristic absorbance of MoS_2 was observed at 398 nm in the UV region. In the hybrid structure, the LSPR band of AuNBPs exhibited a significant redshift (40 nm) from 787 to 827 nm, along with a weak transverse plasmon band at 521 nm.[18,40] The observed redshift and intensity enhancement are indicative of strong plasmon–exciton coupling and
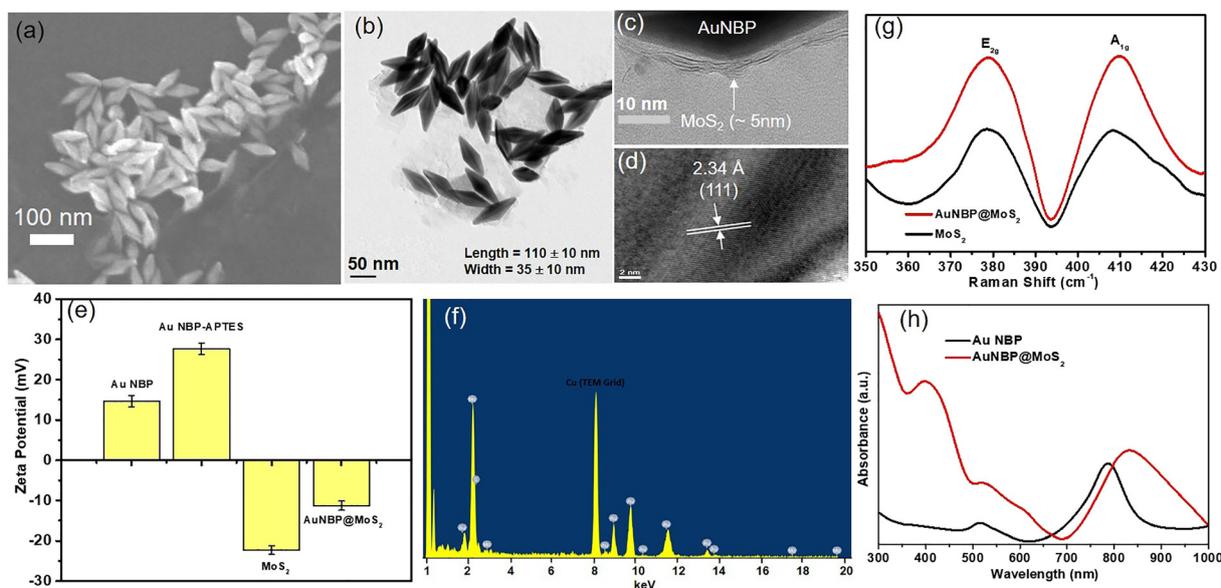

Fig. 1 Structural characterizations and optical property. (a) FESEM image of AuNBP@MoS_2. (b) TEM image and (c) and (d) HRTEM image of AuNBP@MoS_2. (e) Stepwise zeta potential measurements of Au NBPs, MoS_2 and AuNBP@MoS_2. (f) EDS spectra of AuNBP@MoS_2. (g) Raman spectra and (h) UV-vis absorbance spectra of AuNBPs and AuNBP@MoS_2.

electronic interaction between the AuNBPs and MoS_2 NSs in the hybrid system. Additionally, the redshift and broadening suggest successful hybridization, which could optimize light–matter interactions for multifunctional applications.

Photoelectrochemical/photoelectrocatalysis properties of the AuNBP@MoS_2/GC device

The photo-electrochemical/photo-electrocatalysis performance of the AuNBP@MoS_2 nanohybrid modified GC electrode (AuNBP@MoS_2/GC) was then explored in 0.1 M PBS (pH 7.4, 25 °C) with the protection of N_2 using three electrode cell setups under 808 nm LSPR excitation (2 W cm^{-2}). The cyclic voltammetry (CV) curves presented in the image reflect the electrochemical behavior of three different electrode systems – bare GC, AuNBP@MoS_2 modified GC (AuNBP@MOS_2/GC) in the dark, and AuNBP@MoS_2/GC under NIR light illumination (808 nm, 2 W cm^{-2}) (scan rate: 50 mV s^{-1}), and are displayed in Fig. 2a. The bare GC electrode exhibits minimal redox activity, as shown by its nearly featureless curve (Fig. 2a, purple curve). In contrast, the AuNBP@MoS_2/GC electrode in the dark displays three distinct redox features: two oxidation peaks at +0.40 V and +0.83 V, and a reduction peak at −0.65 V (*vs.* Ag/AgCl) (Fig. 2a, black curve), which is in good agreement with our previous reports as well as with earlier reports on AuNS-based electrodes.[34,35,41,42] These redox peaks

arise due to the surface plasmon-assisted electron transfer processes at the AuNBP interface, where the oxidation peaks likely correspond to the formation of gold oxide species or oxidative transformation of adsorbed intermediates (+0.40 V: $Au^0 \rightarrow AuOH/Au_2O_3$, surface oxidation of Au; +0.83 V: $AuOH \rightarrow AuO_x/Au(III)$, further oxidation), while the reduction peak reflects the reduction of these oxidized surface species (−0.65 V: $AuO_x \rightarrow Au^0$, reduction of Au oxide).[35,42] Upon plasmonic excitation using NIR light in the AuNBP@MoS_2/GC system (Fig. 2a, red curve), there is a notable enhancement in all peak currents (∼2-fold: at −0.65 V, from −8.84 μA to −16.57 μA) along with decrease in overpotential (60 mV) by the LSPR effect under 808 nm light illumination. The pronounced electrocatalytic enhancement of the AuNBP@MoS_2/GC electrode under LSPR excitation is attributed to the plasmon-assisted electrochemical reaction (PAER) mechanism, coupled with the photothermal properties of the nanohybrid.[18,29,34] The anisotropic AuNBPs exhibit intense near-field plasmonic effects under resonant illumination, generating a high density of hot electrons that are efficiently injected into the MoS_2 conduction band, thereby driving the PAER process and reducing charge recombination. This plasmonic charge transfer is further amplified by the photothermal effect, as the non-radiative relaxation of LSPR-excited AuNBPs induces localized heating, which lowers the activation barrier for electrochemical
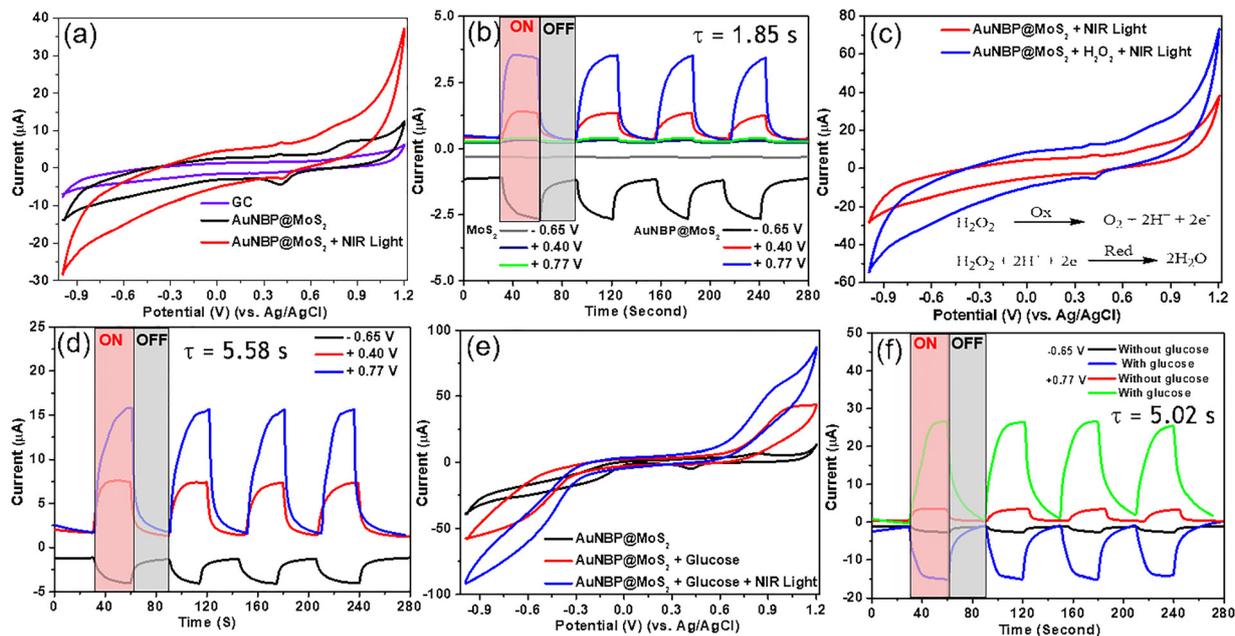

Fig. 2 Electrochemical performance of the AuNBP@MoS_2/GC device. (a) CV curves of bare GC (purple) and AuNBP@MoS_2/GC electrodes with (red) and without (black) NIR light illumination (808 nm, 2 W cm^{-2}) in N_2 saturated 0.1 M PBS, pH 7.4 (scan rate: 50 mV s^{-1}). (b) Current−time response curves of MoS_2 and AuNBP@MoS_2/GC electrodes in N_2 saturated 0.1 M PBS (pH 7.4) at −0.65 V (grey and black), +0.4 V (navy blue and red), and +0.77 V (green and blue), respectively, under periodic OFF/ON of NIR light illumination (808 nm, 2 W cm^{-2}). (c) CV curves of the AuNBP/GC electrode with addition of 1.0 mM H_2O_2 in N_2 saturated 0.1 M PBS (pH 7.4) under NIR light illumination (808 nm, 2 W cm^{-2}). (d) Current−time response curves of the AuNBP@MoS_2/GC electrode with addition of 1.0 mM H_2O_2 into N_2 saturated 0.1 M PBS (pH 7.4) at −0.65 V (black), +0.4 V (red), and +0.77 V (blue) under OFF/ON of NIR light illumination (808 nm, 2 W cm^{-2}). (e) CV curves of the AuNBP@MoS_2/GC electrode in 0.1 M PBS, pH 7.4 (scan rate: 50 mV s^{-1}) without (black), with 1.0 mM glucose (red), and with glucose and under NIR light illumination (808 nm, 2 W cm^{-2}) (blue). (f) Current−time response curves of the AuNBP@MoS_2/GC electrode with and without 1.0 mM glucose in 0.1 M PBS (pH 7.4) at −0.65 V (grey and pink) and +0.77 V (black and red) under periodic OFF/ON of NIR light illumination (808 nm, 2 W cm^{-2}).

reactions and enhances mass transport kinetics. Meanwhile, the 2D MoS$_2$ nanosheets not only facilitate rapid electron extraction and transport due to their high conductivity but also provide abundant edge-active sites for catalytic turnover.[18,29,40] The synergistic interaction between AuNBPs and MoS$_2$ under LSPR illumination thus results in a pronounced enhancement in redox activity, making this hybrid system highly effective for light-assisted electrochemical applications.

To further evaluate the PEC performance, steady-state photocurrent (i–t) measurements were conducted by the chronoamperometric (CA) technique for both MoS$_2$/GC and AuNBP@MoS$_2$/GC electrodes under LSPR excitation (808 nm, 2 W cm^{-2}). The experiments were performed under periodic light ON/OFF switching for 280 s at three distinct bias potentials: -0.65 V, $+0.40$ V, and $+0.77$ V. As shown in Fig. 2b, the MoS$_2$/GC electrode exhibited discernible photocurrent responses upon light illumination at all three applied potentials represented by the grey, green, and navy traces, respectively, likely due to the promotion of exciton separation in MoS$_2$ facilitated by the moderate electric field. However, the relatively low photocurrent density observed indicates a modest PEC performance (Fig. S2).[18] In stark contrast, the AuNBP@MoS$_2$/GC hybrid electrode exhibited a pronounced, rapid increase in photocurrent upon illumination, followed by a quick return to baseline once the light was turned off. This reversible sharp ON/OFF photocurrent response confirms efficient charge separation and robust PEC activity, attributable to the synergistic interaction between MoS$_2$ and plasmonic AuNBPs. The device maintained consistent performance over four consecutive cycles without significant signal degradation, demonstrating excellent photostability. Quantitative analysis revealed that the AuNBP@MoS$_2$/GC electrode delivered up to an 11-fold enhancement in photocurrent at $+0.77$ V (from 0.318 μA to 3.52 μA), compared to the pristine MoS$_2$/GC. Similarly, photocurrent enhancements of approximately 5-fold and 8-fold were observed at $+0.40$ V and -0.65 V, respectively. These results highlight the superior PEC response of the AuNBP@MoS$_2$/GC hybrid system across multiple bias conditions, establishing it as a highly promising candidate for PEC applications. This performance represents a significant advancement over previously reported MoS$_2$-based systems.[18] Further insight into charge carrier dynamics was gained from the CA decay curve, which revealed a hot electron lifetime (τ) of 1.85 s for AuNBP@MoS$_2$/GC under LSPR excitation. This extended lifetime reflects suppressed recombination and sustained carrier availability at the interface, underscoring the role of plasmonic AuNBPs in facilitating efficient energy transfer and charge stabilization within the MoS$_2$ matrix, thereby amplifying the overall PEC performance of the hybrid electrode.

Plasmon-enhanced electrocatalysis towards biologically active species

After fruitful PEC response, the AuNBP@MoS$_2$/GC electrode device was tested for the non-enzymatic electrocatalytic sensing of biologically active species like hydrogen peroxide and glucose as reference species. The CV analysis of the AuNBP@MoS$_2$/GC hybrid electrode under NIR irradiation in a three-electrode system (0.1 M PBS, pH 7.4, 25 °C, N$_2$ protection) reveals rich redox behaviour and compelling electrocatalytic response toward H$_2$O$_2$ as shown in Fig. 2c. In the absence of H$_2$O$_2$ (red curve), the system exhibits anodic and cathodic peaks centred at $+0.40$ V, $+0.83$ V, and -0.65 V as discussed previously. Upon addition of 1.0 mM H$_2$O$_2$, the hybrid electrode demonstrates marked enhancement in both anodic and cathodic peak currents (blue curve): the anodic peak at $+0.77$ V increases from 11.60 μA to 22.62 μA ($\sim$95% enhancement), and the cathodic peak at -0.65 V intensifies from -17.36 μA to -32.18 μA ($\sim$85% enhancement). The peak at $+0.40$ V increases from 7.15 μA to 12.94 μA ($\sim$81% enhancement). The peak separation between oxidation and reduction processes ($\Delta E_p = 104$–142 mV) suggests a quasi-reversible redox system, matching with the ideal Nernstian value (60–200 mV), thus indicating facilitated charge transfer under photo-enhanced conditions.[41] The AuNBP@MoS$_2$/GC electrode was further examined to assess how varying scan rates affect the current peaks associated with H$_2$O$_2$ oxidation and reduction (Fig. S2b and c). The linear relationship observed with the square root of the scan rate suggests rapid catalytic activity, with the electrochemical reaction being predominantly quasi-reversible and diffusion-controlled.[42] The diffusion coefficient (D) for H$_2$O$_2$ oxidation and reduction at the AuNBP@MoS$_2$/GC electrode was determined to be 7.69×10^{-5} cm^2 s^{-1}, which holds significant implications for electrocatalysis.[43] Moreover, the heterogeneous electron transfer rate constant (k^0) based on Laviron's theory was also calculated as 1.17×10^{-1} cm s^{-1}, which also indicates very fast electron transfer.[42] Thus, all these results confirm the catalytic involvement of H$_2$O$_2$ in both oxidation and reduction pathways (reactions are given in the inset of Fig. 2c), underscoring dual-channel electrocatalysis. The increased peak currents and reduced overpotentials under LSPR excitation indicate improved electron transfer kinetics.[38] Peak broadening under light suggests a diffusion-controlled regime, likely aided by plasmon-induced hot-electron generation and localized heating.[23] The amplified currents are attributed to hot-electron transfer from excited AuNBPs to MoS$_2$, along with a photothermal effect that lowers the activation barrier, thereby enhancing surface redox reactions.[18,19,21,44] Additionally, the enhanced anodic-to-cathodic current ratio ($|I_{pa}/I_{pc}|$) in the presence of H$_2$O$_2$ implies higher electrochemical reversibility in the modified environment.[21] The symmetry of the redox couple suggests that electron transfer is not only rapid but also well-coupled to the surface catalytic process.[20] These features are highly beneficial for sensor performance, as they contribute to increased sensitivity, faster response times, and robust detection capability in a non-enzymatic system.

Additionally, the steady-state photocurrent (i–t) response of the AuNBP@MoS$_2$/GC hybrid system was investigated under 808 nm laser illumination (2 W cm^{-2}) in the presence of 1.0 mM H$_2$O$_2$ at applied potentials of -0.650 V, $+0.40$ V, and $+0.77$ V (Fig. 2d), revealing an $\sim$4.5-fold enhancement in photocurrent (from 3.52 μA to 15.85 μA) compared to the

H_2O_2-free system (Fig. 2b), while maintaining reversible ON/OFF switching behaviour due to the PAER mechanism. This significant improvement is attributed to H_2O_2 acting as an efficient electron scavenger, which rapidly consumes photo-generated charge carriers (electrons and holes) at the electrode–electrolyte interface, thereby suppressing recombination and prolonging carrier lifetime. Notably, hot electron lifetime analysis from CA decay curves showed a substantial increase from 1.85 s (without H_2O_2) to 5.58 s in the presence of H_2O_2 under LSPR excitation. This ~3-fold enhancement in carrier lifetime further confirms the role of H_2O_2 in stabilizing photogenerated charges by facilitating fast interfacial redox reactions.[20] The synergistic interplay between plasmonic AuNBPs and MoS_2, coupled with the redox-active nature of H_2O_2, promotes efficient charge separation and transfer, ultimately leading to a markedly amplified and sustained PEC response. These findings underscore the critical importance of suitable electron acceptors in optimizing plasmonic–semiconductor hybrid systems for advanced multi-channel PEC applications.

In a subsequent investigation, we evaluated the glucose biosensing performance of the AuNBP@MoS_2/GC hybrid electrode under LSPR excitation at 808 nm (2 W cm^{-2}), with glucose selected as a representative biomarker for diabetes monitoring.[45] The experimental protocol and electrochemical measurement conditions were consistent with those employed for H_2O_2 detection, except for the introduction of glucose oxidase (GOx; 20 µL, 20 mg L^{-1}) into the PBS electrolyte. As shown in Fig. 2e, CV of the AuNBP@MoS_2/GC electrode in the absence of glucose and without LSPR illumination (dark condition) exhibited distinct redox features with anodic peaks at +0.77 V and +0.40 V and a cathodic peak at −0.65 V (red curve), reflecting the inherent electrochemical activity of the hybrid electrode. Upon the addition of 1.00 mM glucose, the electrode response was significantly amplified, with the anodic peak current increasing from 6.82 µA to 29.37 µA, and the cathodic current from −25.86 µA to −44.20 µA. This enhancement demonstrates the electrode's efficient electrocatalytic response to generated H_2O_2, confirming its high sensitivity toward glucose detection even in the absence of optical excitation. Notably, under LSPR illumination, the peak currents further increased to 55.44 µA (anodic) and −66.28 µA (cathodic), representing an ~8-fold enhancement in current response compared to the baseline condition. This pronounced increase underscores the electrode's plasmon-enhanced PEC sensing capability toward glucose. The sensing mechanism is driven by the oxidation of glucose by GOx, which produces H_2O_2 as a byproduct.[46] The resulting H_2O_2 undergoes redox reactions at the AuNBP@MoS_2/GC surface, generating amplified current signals. The dominant oxidation peak at +0.77 V corresponds to H_2O_2 oxidation, which suppresses the secondary oxidation feature at +0.40 V, indicating a shift in redox dynamics likely due to selective H_2O_2-mediated charge transfer processes under LSPR-induced hot carrier generation. This suggests that the plasmonic activation not only enhances sensitivity but also modulates the electrochemical pathway to favour efficient analyte detection.

The steady-state photocurrent (i–t) response of the AuNBP@MoS_2/GC hybrid system was further examined in the presence of glucose under conditions identical to those used for the H_2O_2 experiments, applying both anodic (+0.77 V) and cathodic (−0.65 V) potentials (Fig. 2f). As anticipated, reversible ON/OFF photocurrent switching was observed at both potentials, reaffirming the superior PEC performance and rapid photoresponse dynamics of the hybrid electrode under LSPR excitation. This enhancement arises from the rapid electro-oxidation and reduction of *in situ* generated H_2O_2, produced *via* the reaction between glucose and GOx, along with efficient separation of plasmon-induced hot charge carriers at the electrode interface.[45] Notably, an ~8-fold increase in photocurrent response (from 3.44 µA to 26.58 µA) was achieved, further validating the exceptional PEC capability of the AuNBP@MoS_2/GC hybrid system. Importantly, hot carrier lifetime (τ) analysis revealed a lifetime of 5.02 s under LSPR excitation in the presence of glucose, significantly longer than the 1.85 s observed in the absence of any redox mediator and comparable to the 5.58 s observed with H_2O_2. This extended lifetime in the glucose-containing system highlights the effective generation and scavenging of H_2O_2 at the interface, which minimizes recombination and sustains hot electron dynamics.[20,21] These findings emphasize the pivotal role of biochemical redox processes in prolonging carrier lifetimes and amplifying PEC signals in plasmonic–semiconductor hybrid architectures.

The PEC responses in all the above-mentioned experiments are found to be more effective at an applied potential of +0.77 V having the maximum enhancement of 11-fold, because it provides an optimal driving force for efficient separation and transfer of photogenerated charge carriers towards the external circuit while minimizing recombination losses at the electrode–electrolyte interface.

Plasmon-enhanced PEC biosensing

Based on prior experimental outcomes, we further investigated the PEC performance of the AuNBP@MoS_2/GC hybrid electrode under LSPR excitation, aiming to develop a nonenzymatic PEC biosensor for biologically relevant species, specifically H_2O_2 and glucose. The biosensing capability was evaluated using the CA technique at selected anodic and cathodic potentials in 0.1 M PBS (pH 7.4, 25 °C, N_2) using the standard three-electrode configuration. As presented in Fig. 3a, a distinct and repeatable stepwise increase in current was observed upon successive addition of H_2O_2 (0–200 mM) to the PBS solution using the AuNBP@MoS_2/GC electrode, both in the absence (black curve) and presence (red curve) of LSPR illumination at an applied potential of −0.65 V. The catalytic current increased significantly under illumination, highlighting the plasmonic enhancement in charge transfer. The corresponding calibration curve (Fig. 3b) demonstrated an initial linear increase in current with H_2O_2 concentration, eventually reaching saturation. Notably, the sensor attained ~95% of its steady-state response within 3–5 s following H_2O_2 addition, indicating fast kinetics. Under LSPR illumination, the device exhibited an excellent linear detection range of 10 µM to 30 mM, with a

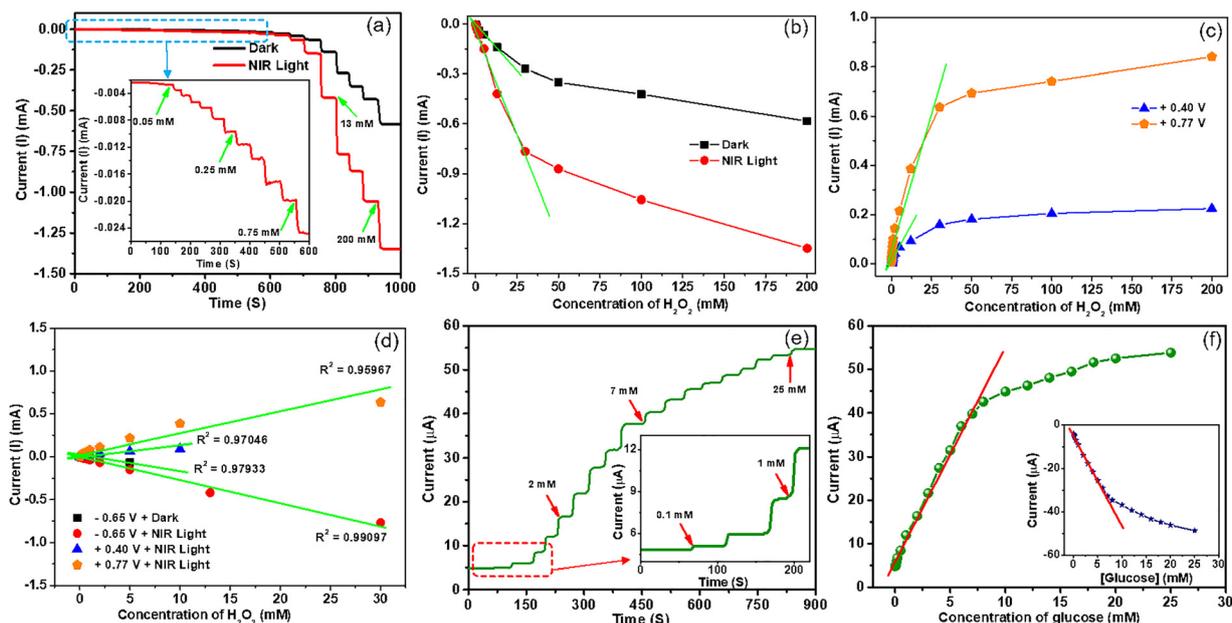**Fig. 3** PEC biosensing activity of the AuNBP@MoS$_2$/GC device towards H$_2$O$_2$ and glucose. (a) Chronoamperometric responses and (b) the corresponding calibration plots of the AuNBP@MoS$_2$/GC electrode in N$_2$ saturated 0.1 M PBS (pH 7.4) at −0.657 V with (red) and without (black) NIR light illumination (808 nm, CW, 2 W cm^{-2}) with consecutive addition of H$_2$O$_2$ from 0 to 200 mM. (c) The calibration plots of catalytic current response *versus* H$_2$O$_2$ concentrations of the AuNBP@MoS$_2$/GC electrode at +0.40 V (blue), and +0.77 V (orange) under NIR light illumination with concentration of added H$_2$O$_2$ from 0 to 200 mM. (d) The corresponding linear fitted calibration plots of current response *versus* H$_2$O$_2$ concentrations of the AuNBP@MoS$_2$/GC electrode at various applied potentials: at −0.65 V in the dark (black), −0.65 V under NIR light illumination (red), +0.40 V under NIR light illumination (blue), and +0.77 V under NIR light illumination (orange). (e) CA responses of the AuNBP@MoS$_2$/GC electrode in 0.1 M PBS at +0.77 V under NIR light illumination with consecutive addition of glucose from 0 to 25 mM. (f) The calibration plots of current response *versus* glucose concentrations of the AuNBP@MoS$_2$/GC electrode at +0.77 V (green) and −0.65 V (navy blue) under NIR light illumination.

correlation coefficient (R^2) of 0.99097, a limit of detection (LOD) of 5 μM (S/N = 3), and a high sensitivity of 376.86 μA mM^{-1} cm^{-2}, as determined from the *i–t* calibration plot (Fig. 3d, green). This performance markedly outperforms the dark condition (no illumination), which showed a linear range of 10 μM to 5 mM, R^2 = 0.97933, and reduced sensitivity, thereby validating the LSPR-assisted PEC enhancement.[47] To further understand the anodic response, CA experiments were conducted under LSPR excitation at two positive potentials: +0.40 V and +0.77 V (Fig. 3c). In both cases, the hybrid electrode maintained rapid response times (3–5 s) and clear stepwise current increases upon H$_2$O$_2$ addition (0–200 mM). At +0.40 V, the device achieved a linear detection range of 10 μM to 10 mM, R^2 = 0.97046, an LOD of 4.9 μM, and a sensitivity of 136.14 μA mM^{-1} cm^{-2} (Fig. 3d, blue). Remarkably, at +0.77 V, the linear range extended to 10 μM–30 mM, with a lower LOD of 1.4 μM, R^2 = 0.97967, and an enhanced sensitivity of 315.00 μA mM^{-1} cm^{-2} (Fig. 3d, orange). The AuNBP@MoS$_2$/GC hybrid electrode, under LSPR excitation, demonstrates remarkable PEC biosensing capabilities for H$_2$O$_2$ detection, outperforming previously reported systems (*e.g.*, AuNR/GC and AuNR@GO/GC) as compared in Table S1.[47]

To extend the biosensing utility of the AuNBP@MoS$_2$/GC hybrid system, we further evaluated its plasmon-assisted PEC response toward glucose detection under optimized conditions. CA measurements were performed in N$_2$-purged 0.1 M PBS (pH 7.4, 25 °C) using a three-electrode setup, under LSPR

illumination to leverage the plasmonic enhancement of AuNBPs. As shown in Fig. 3e, the hybrid electrode displayed a distinct stepwise increase in anodic photocurrent upon successive additions of glucose (0–25 mM) at an applied potential of +0.77 V under LSPR illumination. The current reached a steady state within 4–6 s after each glucose addition, indicating fast and sensitive response kinetics. The corresponding calibration curve (Fig. 3f, green) demonstrated a broad linear detection range of 100 μM to 8 mM, with a correlation coefficient (R^2) of 0.99093, a limit of detection (LOD) of 32.0 μM, and a sensitivity of 23.42 μA mM^{-1} cm^{-2}. These results affirm the robust anodic PEC sensing ability of the AuNBP@MoS$_2$/GC electrode for glucose under physiological conditions.[42,45,47] To probe the versatility of the sensing mechanism, the glucose response was also investigated at a cathodic potential of −0.65 V under similar conditions. The inset of Fig. 3f shows the corresponding calibration plot, with a linear detection range of 100 μM to 8 mM, R^2 = 0.99386, an LOD of 27 μM, and a sensitivity of 8.04 μA mM^{-1} cm^{-2}. While the sensitivity under cathodic bias is lower than that of the anodic condition, it still validates the device's dual-channel sensing capability. The AuNBP@MoS$_2$/GC electrode, under plasmonic excitation, exhibits ultrasensitive and rapid PEC glucose detection in both anodic and cathodic modes, which are also compared in previous reports as listed in Table S2.[42,45,47] The superior sensitivity, broad linear range, and low detection limit underscore its potential as a powerful nonenzymatic PEC biosensor for clinical diagnostics and biomedical applications.

To evaluate the practical applicability of the AuNBP@MoS$_2$/GC biosensor, its operational stability, reproducibility, and anti-interference capability were systematically examined. The device retained approximately 99% of its initial PEC response over five successive measurements, indicating excellent short-term stability. Reproducibility tests across five independently fabricated electrodes yielded a relative standard deviation (RSD) of ~3.5%, confirming consistent sensor fabrication. Long-term stability was further validated by storing the sensor at 4 °C in the dark for 30 days, with negligible loss in PEC activity. The biosensor also demonstrated high selectivity, with minimal current response variation in the presence of common electroactive interferents such as uric acid, dopamine, L-cysteine, and glutathione (each at 0.05 mM) (Fig. S3a).[35] Post-operational TEM analysis (Fig. S4b) confirmed the morphological integrity of the AuNBP@MoS$_2$ architecture after the PEC experiment compared to that of pure AuNBPs (Fig. S4a), underscoring the structural robustness of the hybrid material. Collectively, these results affirm the sensor's high durability, reproducibility, and interference tolerance, underscoring its strong potential for real-world biosensing applications.

PEC biosensing of cancer cells

Inspired by the excellent PEC performance of the AuNBP@MoS$_2$/GC device, we extended our investigation to evaluate its efficacy for real-time biosensing of cancer cells under LSPR excitation (Fig. 4a). Leveraging the enhanced PEC response of the AuNBP@MoS$_2$ interface, we conducted CA measurements to monitor the secretion of H$_2$O$_2$ from live HeLa cells stimulated with the pro-inflammatory agent *N*-formylmethionyl-leucyl-phenylalanine (fMLP) (Fig. 4a).[10,33–35] The secretion of H$_2$O$_2$ from HeLa cancer cells following treatment with fLMP, a pro-inflammatory stimulant, was further validated using the DCFH-DA-based cellular imaging technique. A distinct green fluorescence observed within the cytoplasm confirmed the elevated intracellular levels of H$_2$O$_2$ (Fig. 4b).[35]

Under near-infrared LSPR illumination (808 nm, 2 W cm^{-2}) at an applied potential of −0.65 V, a pronounced increase in cathodic current was recorded upon addition of fMLP to the HeLa cell suspension in PBS (pH 7.4), confirming the effective PEC detection of cell-released H$_2$O$_2$ (Fig. 4c, red trace). Notably, control experiments without fMLP (Fig. 4c, blue trace) or in the absence of cells (Fig. 4c, black trace) exhibited no response, emphasizing the selectivity of the platform for biologically relevant H$_2$O$_2$ signalling. Anti-interference studies with common electroactive species (AA, UA, L-cysteine; 0.05 mM each) showed negligible responses compared to the strong signal from fMLP-stimulated HeLa cells (Fig. S3b), confirming the high selectivity of AuNBP@MoS$_2$/GC for biologically generated H$_2$O$_2$ in complex media.

The observed signal changes at two different applied potentials at −0.65 V (ΔI = 21.3 μA) and +0.77 V (ΔI = 24.5 μA), as shown in Fig. 4d, correspond to an estimated H$_2$O$_2$ concentration of approximately 1.24 mM, with each HeLa cell secreting
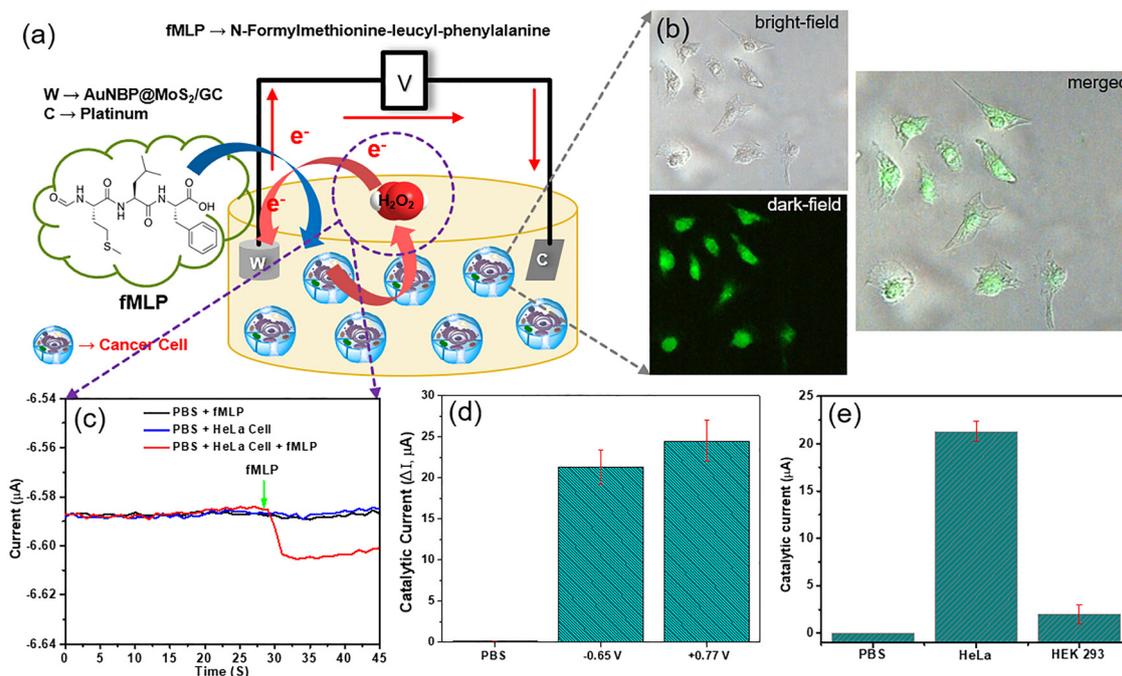

Fig. 4 Sensor device for cancer cell detection. (a) Schematic illustration of PEC cancer cell detection by the AuNBP@MoS$_2$/GC electrode under NIR light illumination. (b) CLSM images of HeLa cells incubated with fLMP followed by treatment with DCFH–DA for determination of elevated intracellular H$_2$O$_2$ levels. (c) CA responses of the AuNBP@MoS$_2$/GC electrode device in N$_2$ saturated 0.1 M PBS (pH 7.4) solution through biosensing H$_2$O$_2$ released from HeLa cells with addition of 5 mM fMLP at an applied potential of −0.65 V. (d) Comparison of generated current response for cancer cell detection using the AuNBP@MoS$_2$/GC electrode device as controlled and at −0.65 V and +0.77 V applied potentials. (e) Comparison of cellular assay by the AuNBP@MoS$_2$/GC device for detection of cancerous cells (HeLa) compared to a normal cell (HEK 293).

$\sim$138 amol of H_2O_2, values that are consistent with those reported for stimulated cancer cells.[35,48] The average number of H_2O_2 molecules (N_0) secreted per HeLa cell was estimated to be 8.32×10^8, which aligns well with previously reported data, further validating the accuracy of the biosensing approach.[49] Importantly, under identical conditions, normal human embryonic kidney (HEK 293) cells elicited a negligible catalytic current response (Fig. 4e), clearly distinguishing them from the pronounced signal observed for HeLa cells.[35] The AuNBP@-MoS$_2$/GC biosensor demonstrates excellent sensitivity, selectivity and stability for real-time H_2O_2 detection, showcasing strong potential for cancer diagnostics and redox biology applications.

Mechanism of direct plasmon-enhanced photoelectrocatalysis (PEC)

To unravel the underlying mechanism responsible for the significantly improved PEC performance of the AuNBP@-MoS$_2$/GC hybrid electrode under LSPR excitation, a series of complementary electrochemical and optical experiments were performed, supported by computational simulations. These efforts collectively reveal how plasmonic nanostructures can directly mediate and enhance charge transfer kinetics and catalytic efficiency in a hybrid PEC platform.

Electrochemical impedance spectroscopy (EIS) was employed to assess the charge transfer characteristics across different configurations (Fig. 5a). Bare GC exhibited a large semicircular Nyquist profile with a high charge transfer resistance (R_{ct} = 2197 Ω), indicative of inefficient electron transport (Fig. 5a, black curve).[35] Upon modification with AuNBP@MoS$_2$, R_{ct} decreased to 1470 Ω in the dark, affirming improved conductivity due to the formation of an efficient electron

pathway. Remarkably, under 808 nm LSPR illumination (2 W cm^{-2}), R_{ct} further dropped to 697 Ω, validating enhanced interfacial charge separation and accelerated transport, a direct consequence of hot carrier injection from excited AuNBPs into the MoS$_2$ matrix.[30,35] The schematic equivalent circuit confirms this evolution of impedance behaviour. The observed light-induced enhancement reflects the synergistic coupling between the plasmonic core and the semiconducting shell, enabling a cascade of rapid photoinduced charge separation and migration events. Additionally, the open-circuit potential (OCP) response under light–dark cycling displays a clear shift ($\sim$25 μA), further substantiating the generation and successful transfer of photoexcited hot electrons to MoS$_2$, followed by efficient conduction to the external circuit.[44]

Photo-response analysis as a function of illumination wavelength (Fig. 5b) showed a peak photocurrent at 827 nm, coinciding with the LSPR maximum of the AuNBP@MoS$_2$ system. This resonance matching confirms the dominance of plasmonic excitation over bulk photothermal or bandgap-mediated photoactivity in driving PEC enhancements.[44,45] Furthermore, the photocurrent response scaled linearly with increasing laser intensity (0 to 2.0 W cm^{-2}) (Fig. 5c), peaking at 12.27 μA. This behaviour suggests a higher generation rate of non-equilibrium hot electrons at elevated photon flux, thereby improving both the probability of interfacial charge transfer and the charge carrier lifetime. This linear correlation is a hallmark of hot-carrier-involved mechanisms rather than simple thermal heating effects.[35,44,45] To further validate this, measurements were conducted in the presence of ethanol (EtOH) as a hole scavenger (Fig. 5d), which resulted in a markedly enhanced current response. This enhancement is attributed to effective
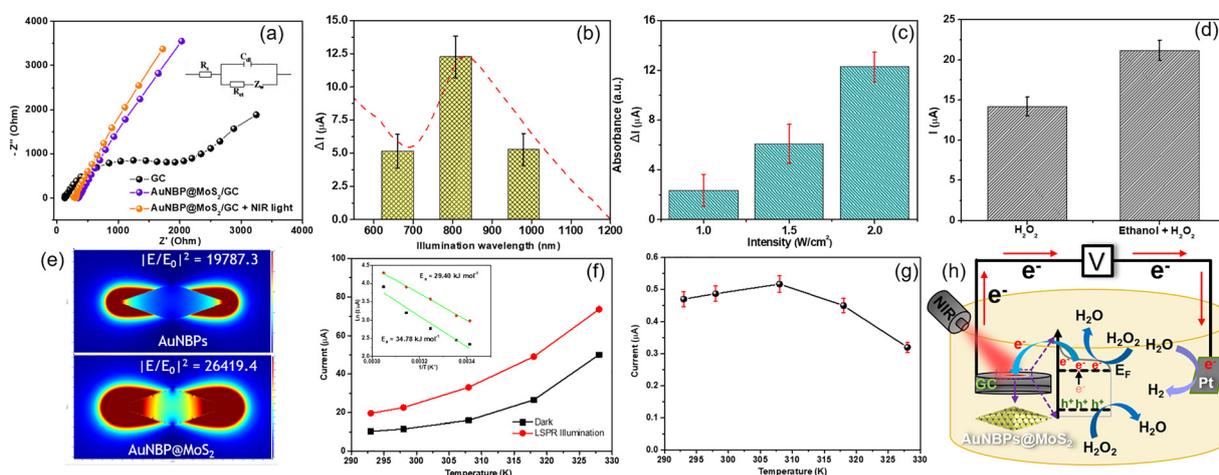

Fig. 5 Investigation of the mechanism behind superior PEC properties. (a) Nyquist plots of bare GC (black curve) and AuNBP@MoS$_2$/GC electrodes in 0.1 M PBS containing 5 mM Fe(CN)$_6^{4+/3+}$ with (orange) and without (violet) NIR light illumination (808 nm, 2 W cm^{-2}). (b) Catalytic peak currents (ΔI) of the AuNBP@MoS$_2$/GC electrode in 0.1 M PBS at +0.77 V under variable wavelength illumination of the NIR light source (2 W cm^{-2}). (c) Catalytic peak currents (ΔI) of the AuNBPs@MoS$_2$/GC electrode in 0.1 M PBS at +0.77 V with an adaptable irradiation intensity of 808 nm NIR light. (d) Catalytic peak currents of the AuNBP@MoS$_2$/GC electrode in 0.1 M PBS at +0.77 V with H_2O_2 in the absence and presence of EtOH. (e) FDTD simulations and local field enhancement intensity of AuNBP and AuNBP@MoS$_2$ obtained at an incident excitation wavelength of 808 nm. (f) Plot of peak current vs. temperature with laser light on and off for electrochemical oxidation/reduction of H_2O_2 by AuNBP@MoS$_2$/GC. Inset: plot of ln(I) vs. reciprocal of temperature ($1/T$). (g) The ratio of (($I - I_0$)/I) at different temperatures, where I_0 is the peak current in the dark and I is the peak current of H_2O_2 electrochemical oxidation/reduction under LSPR excitation. (h) Proposed mechanism for the superior PEC activity of the AuNBP@MoS$_2$/GC device under LSPR illumination.

suppression of electron–hole recombination, as EtOH preferentially consumes photogenerated holes, thus promoting improved charge carrier separation and utilization.

To visualize the spatial distribution and amplification of the localized electromagnetic (EM) fields, finite-difference time-domain (FDTD) simulations were conducted (Fig. 5e). For bare AuNBPs, intense near-field hot spots were observed at the bipyramidal tips, yielding a field enhancement factor $|E/E_0|^2$ of 19 787.3. In contrast, the AuNBP@MoS$_2$ heterostructure exhibited a significantly elevated $|E/E_0|^2$ of 26 419.4, corresponding to ∼1.3-fold enhancement.[40] This increase arises from plasmonic coupling and dielectric confinement at the metal–semiconductor interface. MoS$_2$ not only acts as a charge acceptor but also modulates the local dielectric environment, promoting stronger field localization and, consequently, more efficient hot-electron injection into its conduction band. This improved EM confinement directly correlates with the observed photocurrent enhancements and underscores the critical role of anisotropic nanogeometry in dictating light–matter interaction strength.[35,40]

To delineate the thermally and non-thermally activated pathways towards H$_2$O$_2$ oxidation/reduction, temperature-dependent electrochemical measurements were carried out (Fig. 5f and g). The apparent activation energy (E_a) under dark conditions was calculated to be 41.2 kJ mol^{-1}, which significantly decreased to 33.7 kJ mol^{-1} upon LSPR illumination. This reduction in E_a under NIR light underscores the facilitative role of hot carriers in overcoming kinetic barriers to electron transfer.[44] Interestingly, while the photocurrent enhancement $[(I - I_0)/I]$ initially increases with temperature (298–308 K), it starts to decline at higher temperatures (318–328 K), implying a mechanistic transition. At lower temperatures, photothermal effects dominate by increasing charge mobility, whereas at elevated temperatures, the hot carrier contribution becomes the primary driver of PEC enhancement.[44] This temperature-dependent crossover reaffirms a dual mechanism – wherein both LSPR-induced heating and hot carrier effects synergistically operate, with the latter being more decisive at higher operating temperatures.[44]

We explicitly quantify and correlate three key mechanistic parameters—hot carrier lifetime, interfacial energetics, and structure–activity relationships—based on combined electrochemical and simulation data. The hot carrier lifetime (τ) extends from 1.85 s to 5.58 s with redox scavenging, the activation energy (E_a) decreases from 41.2 to 33.7 kJ mol^{-1} under LSPR illumination, and FDTD simulations reveal that the anisotropic AuNBP geometry yields a maximum near-field enhancement ($|E/E_0|^2$) of 26 419.4, all of which directly contribute to the observed PEC enhancement.

Thus, the most plausible mechanism underlying the direct plasmon-enhanced PEC activity of the AuNBPs@MoS$_2$/GC hybrid system under 808 nm NIR light illumination is schematically depicted in Fig. 5h. Upon LSPR excitation of the anisotropic AuNBPs, electrons from the d-band are excited to higher energy states above the Fermi level, creating energetic hot electrons and corresponding hot holes.[18–21,27] Due to the sharp

tips of AuNBPs, intense electromagnetic "hot-spots" are formed where hot carrier generation and localized photothermal effects are maximized.[37] These hot electrons can be injected into the conduction band of MoS$_2$, facilitated by suitable band alignment and a low Schottky barrier, followed by transfer to the GC electrode and through the external circuit under an applied bias, leading to an enhanced PEC signal.[18,20] Simultaneously, hot holes accumulate on the AuNBP surface, causing a downward shift in the Fermi level, thereby improving their oxidative power.[21] This dual process enables both the oxidation and reduction of H$_2$O$_2$ at the photoactive interface: hot holes oxidize H$_2$O$_2$, generating reactive oxygen species like •OH and •OOH radicals, while the accumulated hot electrons can reduce H$_2$O$_2$, thus facilitating bidirectional electrocatalysis.[20,21,35,47] In biosensing applications, H$_2$O$_2$ may either be present directly or produced from oxidation of glucose by GOX, making the system suitable for PEC biosensing of both H$_2$O$_2$ and glucose.[21,45,47] Furthermore, the NIR-induced photothermal effect increases the local temperature, improving charge carrier mobility and lowering activation energy barriers for redox reactions.[44,45] Therefore, the enhanced PEC response arises from a synergistic combination of LSPR-generated hot carriers, bidirectional electrocatalysis of H$_2$O$_2$, effective charge separation, and photothermal facilitation, collectively making AuNBPs@MoS$_2$/GC an efficient PEC platform for sensitive and amplified biosensing applications.

Plasmon-accelerated HER activity

The photo-electrocatalytic hydrogen evolution reaction (HER) performance of the plasmonic AuNBP@MoS$_2$/GC hybrid electrode was systematically investigated using a standard three-electrode configuration in N$_2$-saturated 0.5 M H$_2$SO$_4$ electrolyte at 30 °C. LSPR excitation was achieved using an 808 nm laser source with an intensity of 2 W cm^{-2}. The linear sweep voltammetry (LSV) curves recorded under various conditions are shown in Fig. 6a. The GC electrode modified solely with exfoliated MoS$_2$ exhibited limited HER activity, as evidenced by a high onset potential of approximately −0.31 V vs. the reversible hydrogen electrode (RHE) under dark conditions (Fig. 6a, grey curve). This is consistent with the inherently poor electrical conductivity and basal-plane inactivity of pristine semiconducting MoS$_2$.[18] However, incorporation of AuNBPs into the MoS$_2$ matrix (AuNBP@MoS$_2$/GC) markedly improved the catalytic performance. In the absence of illumination, the hybrid electrode showed a positive shift in the onset potential to −0.28 V (ΔE = 33 mV), suggesting enhanced charge transport and favourable interfacial electronic interactions between Au and MoS$_2$ (Fig. 6a, black curve).[28] Under LSPR excitation, a further anodic shift in the onset potential to −0.19 V was recorded (ΔE = 88 mV), accompanied by a substantial reduction in overpotential at −10 mA cm^{-2}, from −0.513 V to −0.354 V (ΔE = 159 mV) (Fig. 6a, red curve). This significant improvement highlights the effective role of plasmon-induced hot electron injection in enhancing HER kinetics (Table S3).[18,28–31,50–53] Notably, a sharp increase in cathodic current density was observed upon laser irradiation
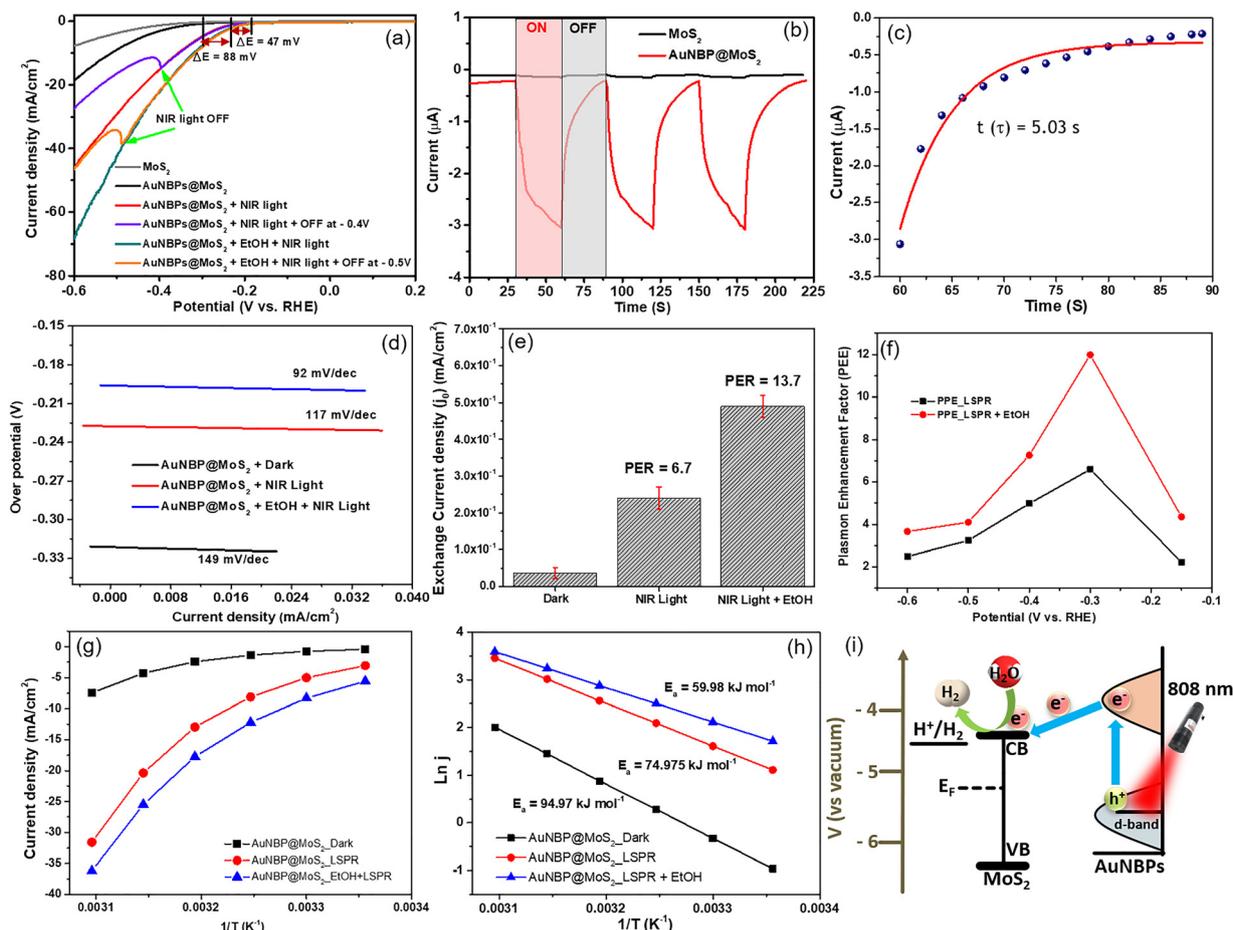
Fig. 6 Plasmon accelerated HER performance. (a) LSV polarization curves of MoS$_2$/GC (grey curve) and AuNBP@MoS$_2$/GC electrodes in N$_2$ saturated 0.5 M H$_2$SO$_4$ (30 °C, scan rate: 10 mV s^{-1}) with (red curve), without (black curve) and sudden off (purple curve) of NIR light illumination (808 nm, 2 W cm^{-2}) as well as with ethanol (10%) under NIR light illumination (green curve) and sudden off (blue curve) of NIR light. (b) Current–time response curves of MoS$_2$/GC (black) and AuNBP@MoS$_2$/GC electrodes (red) in N$_2$ saturated 0.5 M H$_2$SO$_4$ under periodic ON/OFF of NIR light. (c) Plot of current *vs.* time, with an exponential fit to the decay for the AuNBP@MoS$_2$/GC device after switch off of NIR light. (d) Tafel plots of AuNBP@MoS$_2$ with (red), without (black) NIR light illumination, and in the presence of ethanol with NIR light illumination (808 nm, 2 W cm^{-2}). (e) Plot of exchange current density (j_0) under three different conditions: AuNBP@MoS$_2$ in the dark, under LSPR illumination and under LSPR illumination in the presence of EtOH. (f) Plot of plasmon enhancement factor with variable potentials for AuNBP@MoS$_2$ under LSPR illumination with and without EtOH. (g) Current density *vs.* inverse temperature at a fixed potential of −0.3 V for AuNBP@MoS$_2$ in the dark, under LSPR illumination and under LSPR illumination in the presence of EtOH. (h) Arrhenius plots: plot of ln(j) *vs.* reciprocal of temperature (1/T) for AuNBP@MoS$_2$ in the dark, under LSPR illumination and under LSPR illumination with EtOH. (i) Schematic energy diagram showing the direct plasmon-enhanced HER mechanism in AuNBP@MoS$_2$.

at −0.15 V, which promptly declined upon switching off the light (Fig. 6a, purple curve), demonstrating rapid and reversible photocurrent generation. The minimal residual current after laser off suggests negligible thermal effects, confirming that hot electrons, generated through non-radiative plasmon decay, are the primary contributors to enhanced HER activity.[18,20] Further improvement was achieved by introducing ethanol as a sacrificial hole scavenger. The onset potential further shifted to −0.14 V ($\Delta E = 47$ mV) and the overpotential at −10 mA cm^{-2} decreased to −0.316 V (Fig. 6a, green curve). This enhancement likely arises from suppressed electron–hole recombination and more effective utilization of photo-excited charge carriers.[18,35,50–53] Interestingly, even after switching off the light at −0.4 V, the current did not completely revert to the dark baseline (Fig. 6a, blue curve), possibly due to residual

photogenerated carrier dynamics or localized heating effects.[35] These enhancements compare favourably or even exceed those observed in analogous plasmonic systems, such as AuNRs@MoS$_2$ (onset at ∼−0.16 V) and AuNPs@rGO hybrids, further demonstrating the advantage of the anisotropic bipyramidal geometry in concentrating the electromagnetic field and facilitating charge transfer (Table S3).[18,29,50] Moreover, the comparative HER tests with commercial Pt/C (0.5 M H$_2$SO$_4$) showed superior HER activity (an onset potential of −0.004 V and a Tafel slope of 26.3 mV dec^{-1}), while our AuNBP@MoS$_2$ exhibited a competitive onset (−0.14 V) and the performance gap narrowed markedly due to hot carrier contributions under LSPR illumination (Fig. S5a). A long-term durability test (1000 LSV cycles, Fig. S5b) was also conducted for the AuNRs@MoS$_2$ hybrid system, which revealed minimal

degradation in HER activity, confirming the structural and electrochemical stability of the hybrid electrode under operational conditions.

The CA measurement was performed at a constant potential of -0.19 V to examine the photo-response dynamics (Fig. 6b). Upon illumination, the photocurrent surged from -0.22 μA to -3.06 μA, representing a 14-fold increase. The current returned to its baseline after the light was turned off and showed excellent reproducibility across multiple cycles, affirming the optical stability and reversibility of the AuNBP@MoS$_2$ hybrid electrode. In contrast, the MoS$_2$-only electrode exhibited negligible photocurrent under identical conditions (Fig. 6b, black curve), underscoring the critical role of AuNBPs in harvesting NIR light and driving the catalytic process.[18] Moreover, analysis of the CA decay curve revealed a hot carrier lifetime (τ) of 5.03 s for the AuNBP@MoS$_2$ system under LSPR excitation (Fig. 6c). This prolonged carrier lifetime indicates efficient suppression of recombination and sustained hot electron availability at the electrode surface, which is vital for enhancing the HER performance. The extended lifetime facilitates more effective interfacial electron transfer to protons in the electrolyte, thereby improving the kinetics and overall efficiency of the HER process under photoelectrochemical conditions.[18,50–53]

The Tafel slope analysis further elucidates the mechanistic shift in HER kinetics. Under dark conditions, the Tafel slope of 149 mV dec^{-1} suggests that the Volmer step (H$^+$ adsorption) is rate-limiting, consistent with low hydrogen coverage (Θ_H) on the catalyst surface (Fig. 6d, black line). Upon LSPR illumination, the Tafel slope decreases to 117 mV dec^{-1} (Fig. 6d, red line), indicating a partial transition toward the Heyrovsky step (electrochemical desorption), implying an increased Θ_H due to enhanced electron availability.[18] Remarkably, the introduction of ethanol as a hole scavenger further decreases the Tafel slope to 92 mV dec^{-1} (Fig. 6d, blue line), closely approaching the theoretical value associated with the Tafel recombination mechanism, indicative of a near-saturated surface coverage of hydrogen intermediates.[50–53] This phenomenon highlights the synergistic contribution of plasmonic excitation and efficient hole scavenging to facilitate charge carrier separation and inhibit electron–hole recombination, thereby significantly enhancing the kinetics of the hydrogen evolution reaction.

Electrochemical double layer capacitance (C_{dl}) measurements were conducted to evaluate the electrochemically active surface area (ECSA) of the AuNBP@MoS$_2$ catalyst. In the absence of LSPR excitation, the C_{dl} was found to be 4.6 mF cm^{-2}, indicating limited surface charge accumulation.[50,54,55] Under 808 nm LSPR illumination, the C_{dl} increased significantly to 12.9 mF cm^{-2}, suggesting a substantial enhancement in accessible active sites.[50,54,55] This increase is attributed to plasmon-induced effects such as hot electron injection, localized electric field enhancement, and improved interfacial charge distribution, confirming that LSPR excitation effectively activates the catalyst surface for improved electrochemical performance.

The kinetic analysis of AuNBP@MoS$_2$/GC under varying conditions (dark, LSPR illumination, and LSPR with ethanol)

provides compelling evidence for plasmon-mediated enhancement of the HER. The exchange current density (j_0), a key parameter reflecting intrinsic catalytic activity, exhibits a substantial increase from 0.036 mA cm^{-2} (dark) to 0.2418 mA cm^{-2} (LSPR illumination) and further to 0.455 mA cm^{-2} (LSPR + EtOH), corresponding to plasmonic enhancement ratios of 6.7 and 13.7, respectively (Fig. 6e).[29] This dramatic improvement is attributed to the injection of hot electrons from AuNBPs into the conduction band of MoS$_2$ upon resonant excitation at 808 nm, which aligns with the LSPR of AuNBPs. The injected electrons increase the charge carrier density in MoS$_2$, effectively modulating its Fermi level closer to the thermodynamic potential for the HER, thereby reducing the overpotential required for proton reduction.[19,20] The plasmonic enhancement factor (PEF) analysis at different applied potentials reveals that the highest enhancement (PEF = 12-fold) occurs at -0.3 V *vs.* RHE under LSPR in the presence of EtOH, demonstrating that the plasmonic effect is most pronounced at moderate overpotentials where charge transfer kinetics dominate (Fig. 6f).[19] At higher overpotentials (-0.5 to -0.6 V), the PEF decreases due to mass transport limitations, but the overall current density remains significantly higher than that under dark conditions, highlighting the sustained catalytic advantage of plasmonic excitation.[20]

The activation energy (E_a) analysis provides additional mechanistic insights. The E_a for the HER decreases from 94.97 kJ mol^{-1} (dark) to 74.975 kJ mol^{-1} (LSPR illumination) and further to 59.98 kJ mol^{-1} (LSPR + EtOH), confirming that plasmonic hot electron injection and hole scavenging synergistically lower the energy barrier for proton reduction (Fig. 6g and h).[18] The reduction in E_a is consistent with the observed enhancement in exchange current density and Tafel kinetics, reinforcing the role of plasmonic excitation in facilitating charge transfer and surface reaction dynamics. To gain deeper mechanistic understanding, the turnover frequency (TOF) of active sites on the AuNBP@MoS$_2$/GC device was evaluated under three distinct conditions: in the dark, under LSPR illumination, and under LSPR illumination in the presence of EtOH. In the absence of illumination, the HER TOF was determined to be 0.40 s^{-1}. Upon excitation of the LSPR mode, the TOF increased significantly to 2.65 s^{-1}, corresponding to an ~ 6.6-fold enhancement, attributable to the injection of plasmon-generated hot electrons into MoS$_2$.[18] Remarkably, in the presence of both LSPR excitation and EtOH, the TOF further increased to 4.82 s^{-1}, representing an overall ~ 12-fold enhancement relative to the dark conditions. The TOF values are in good agreement as calculated for plasmon based MoS$_2$ materials exhibiting high catalytic activity for the HER.[18,35,50–53] This substantial improvement highlights the synergistic effect of hot electron generation and effective hole scavenging in suppressing charge recombination and accelerating HER kinetics.

The schematic diagram as displayed in Fig. 6i thus illustrates the proposed mechanism of the enhanced HER performance of the AuNBP@MoS$_2$/GC system under near-infrared (808 nm) laser excitation, which activates the LSPR of the

AuNBPs. Upon excitation, the LSPR decay of AuNBPs generates energetic non-equilibrium charge carriers, namely hot electrons and hot holes within the metal nanostructure.[19] These hot electrons are efficiently injected into the conduction band (CB) of MoS_2 due to the favourable band alignment and relatively low Schottky barrier at the Au–MoS_2 interface, creating a dynamic charge-separated state with the hot electrons localized in the CB of MoS_2 and holes retained within the Au d-band region.[18] This electron transfer raises the Fermi level of MoS_2, thereby making its energy level more closely aligned with the hydrogen redox potential (H^+/H_2), which results in a lowered overpotential requirement for the HER.[20] Simultaneously, the presence of these photoexcited electrons in MoS_2 enhances the carrier density and conductivity of the semiconductor, leading to an overall improvement in photocurrent density and catalytic turnover. Moreover, the electromagnetic field enhancement around the sharp tips of the AuNBPs intensifies the local electric field, promoting near-field effects that further accelerate interfacial charge transfer kinetics and may contribute to mild photothermal heating.[19] These combined effects facilitate the electrochemical reduction of protons at the MoS_2 surface, enabling efficient evolution of molecular hydrogen (H_2). Importantly, in the presence of a sacrificial hole scavenger such as ethanol, the recombination of hot electrons and holes is significantly suppressed, which leads to a further enhancement of HER kinetics.[18] Collectively, the AuNBP@MoS_2/GC system demonstrates outstanding PEC activity, robust cycling stability, and efficient light-to-chemical energy conversion, making it a compelling candidate for next-generation, LSPR-assisted hydrogen evolution applications.

Conclusions

We report the design of a plasmonic Au nanobipyramid@MoS_2 (AuNBP@MoS_2) nanohybrid that integrates LSPR-driven hot electron generation with 2D semiconductor charge transport for high-performance photoelectrochemical applications. The study establishes a clear mechanistic link between extended hot carrier lifetime (up to 5.58 s), reduced activation energy ($41.2 \rightarrow 33.7$ kJ mol^{-1}), and anisotropic plasmonic field enhancement ($|E/E_0|^2 = 26\,419.4$) as the key drivers of the exceptional PEC performance. The AuNBP@MoS_2/GC electrode enabled dual channel non-enzymatic detection of H_2O_2 with a broad linear range (10 μM–30 mM), ultra-low detection limit (1.4 μM), and high sensitivity (376.86 μA mM^{-1} cm^{-2}). For glucose, it achieved a linear range of 100 μM–8 mM, LOD of 27 μM, and sensitivity of 23.42 μA mM^{-1} cm^{-2}. The device also selectively detected cancer cells *via* real-time monitoring of secreted H_2O_2. In HER studies, the hybrid electrode showed remarkable improvement with a low onset potential (−0.14 V), Tafel slope of 92 mV dec^{-1}, and up to 14-fold photocurrent enhancement under LSPR. These enhancements stem from synergistic hot electron injection, photothermal activation, and MoS_2-mediated catalysis. Overall, this work presents a robust, multifunctional platform for biosensing, cancer diagnostics, and photo-enhanced hydrogen evolution, offering new pathways for LSPR-assisted energy and biomedical technologies.

Author contributions

S. K. M. and D. H. K. conceived and supervised the project. D. D. carried out the synthesis, structural characterization, and electrochemical experiments. R. M. performed the photoelectrochemical and hydrogen evolution studies. R. C. M. assisted in material characterization and data analysis. S. Yu established and provided the protocol for the synthesis of core@ shell AuNBP@MoS_2. D.-I. Won supported the measurement and interpretation of catalytic and electrochemical properties. D. D. and R. M. co-wrote the initial manuscript draft. S. K. M. and D. H. K. finalized the manuscript and provided conceptual insights. All authors discussed the results and approved the final version of the manuscript.

Conflicts of interest

The authors declare no competing financial interest.

Data availability

All data supporting the findings of this study within the article and its supplementary information (SI) are available. Supplementary information is available. The Electronic Supplementary Information (ESI) includes comparative tables for H_2O_2 and glucose biosensing and HER performance, supporting FESEM/TEM and electrochemical data, detailed kinetic and activation energy calculations related to Au–MoS_2 and plasmon-enhanced electrocatalysis. See DOI: **https://doi.org/10.1039/d5nh00491h**.

Acknowledgements

References

1 C. C. Winterbourn, Reconciling the chemistry and biology of reactive oxygen species, *Nat. Chem. Biol.*, 2008, **4**, 278–286.

2 Y. Liu, X. Liu, Z. Guo, Z. Hu, Z. Xue and X. Lu, Horseradish peroxidase supported on porous graphene as a novel sensing platform for detection of hydrogen peroxide in living cells sensitively, *Biosens. Bioelectron.*, 2017, **87**, 101–107.

3 W. Chen, S. Cai, Q.-Q. Ren, W. Wen and Y.-D. Zhao, Recent advances in electrochemical sensing for hydrogen peroxide: a review, *Analyst*, 2012, **137**, 49–58.

4 Y. Shu, J. Chen, Q. Xu, Z. Wei, F. Liu, R. Lu, S. Xu and X. Hu, MoS_2 nanosheet–Au nanorod hybrids for highly sensitive amperometric detection of H_2O_2 in living cells, *J. Mater. Chem. B*, 2017, **5**, 1446–1453.

5 T. Ahmad, A. Iqbal, S. A. Halim, J. Uddin, A. Khan, S. El Deeb and A. Al-Harrasi, Recent advances in electrochemical sensing of hydrogen peroxide (H_2O_2) released from cancer cells, *Nanomaterials*, 2022, **12**, 1475.

6 J. Meier, E. M. Hoferber, J. A. Stapleton and N. M. Iverson, Hydrogen peroxide sensors for biomedical applications, *Chemosensors*, 2019, **7**, 64.

7 R. Wilson and A. P. F. Turner, Glucose oxidase: an ideal enzyme, *Biosens. Bioelectron.*, 1992, **7**, 165–185.

8 H. Teymourian, A. Barfidokht and J. Wang, Electrochemical glucose sensors in diabetes management: an updated review (2010–2020), *Chem. Soc. Rev.*, 2020, **49**, 7671–7709.

9 C. Lennicke, J. Rahn, R. Lichtenfels, L. A. Wessjohann and B. Seliger, Hydrogen peroxide – production, fate and role in redox signaling of tumor cells, *Cell Commun. Signaling*, 2015, **13**, 39.

10 T. Wang, H. Zhu, J. Zhuo, Z. Zhu, P. Papakonstantinou, G. Lubarsky, J. Lin and M. Li, Biosensor based on ultrasmall MoS_2 nanoparticles for electrochemical detection of H_2O_2 released by cells at the nanomolar level, *Anal. Chem.*, 2013, **85**, 10289–10295.

11 S. K. Maji, S. Sreejith, A. K. Mandal, X. Ma and Y. Zhao, Immobilizing gold nanoparticles in periodic mesoporous silica covered reduced graphene oxide: a hybrid material for cancer cell detection through hydrogen peroxide sensing, *ACS Appl. Mater. Interfaces*, 2014, **6**, 13648–13656.

12 M. S. Dresselhaus and I. L. Thomas, Alternative energy technologies, *Nature*, 2001, **414**, 332–337.

13 J. A. Turner, Sustainable hydrogen production, *Science*, 2004, **305**, 972–974.

14 J. Greeley, T. F. Jaramillo, J. Bonde, I. Chorkendorff and J. K. Nørskov, Computational high-throughput screening of electrocatalytic materials for hydrogen evolution, *Nat. Mater.*, 2006, **5**, 909–913.

15 H. Vrubel and X. Hu, Molybdenum boride and carbide catalyze hydrogen evolution in both acidic and basic solutions, *Angew. Chem., Int. Ed.*, 2012, **51**, 12703–12706.

16 M. A. Lukowski, A. S. Daniel, F. Meng, A. Forticaux, L. S. Li and S. Jin, Enhanced hydrogen evolution catalysis from chemically exfoliated metallic MoS_2 nanosheets, *J. Am. Chem. Soc.*, 2013, **135**, 10274–10277.

17 X. Huang, Z. Zeng, S. Bao, M. Wang, X. Qi, Z. Fan and H. Zhang, Solution-phase epitaxial growth of noble metal nanostructures on dispersible single-layer molybdenum disulfide nanosheets, *Nat. Commun.*, 2013, **4**, 1444.

18 Y. Shi, J. Wang, C. Wang, T.-T. Zhai, W.-J. Bao, J.-J. Xu, X.-H. Xia and H.-Y. Chen, Hot electron of Au nanorods activates the electrocatalysis of hydrogen evolution on MoS_2 nanosheets, *J. Am. Chem. Soc.*, 2015, **137**, 7365–7370.

19 J. Zhao, S. Xue, R. Ji, B. Li and J. Li, Localized surface plasmon resonance for enhanced electrocatalysis, *Chem. Soc. Rev.*, 2021, **50**, 12070–12103.

20 H. Tang, C.-J. Chen, Z. Huang, J. Bright, G. Meng, R.-S. Liu and N. Wu, Plasmonic hot electrons for sensing, photodetection, and solar energy applications: a perspective, *J. Chem. Phys.*, 2020, **152**, 220901.

21 Y. Zhang, W. Guo, Y. Zhang and W. D. Wei, Plasmonic photoelectrochemistry: in view of hot carriers, *Adv. Mater.*, 2021, **33**, 2006654.

22 Y. Kang, S. Najmaei, Z. Liu, Y. Bao, Y. Wang, X. Zhu, N. J. Halas, P. Nordlander, P. M. Ajayan, J. Lou and Z. Fang, Plasmonic hot electron induced structural phase transition in a MoS_2 monolayer, *Adv. Mater.*, 2014, **26**, 6467–6471.

23 C. Wang, X.-P. Zhao, Q.-Y. Xu, X.-G. Nie, M. R. Younis, W.-Y. Liu and X.-H. Xia, Importance of hot spots in gold nanostructures on direct plasmon-enhanced electrochemistry, *ACS Appl. Nano Mater.*, 2018, **1**, 5805–5811.

24 S. Yu, D. Jang, H. Kang, H. Lee, J. Park, H. Choi, W.-T. Huang, M. Kim, K. Chung, D. J. Ahn, R.-S. Liu, J. Bang, S. Kim, L. P. Lee and D. H. Kim, Photoinduced plasmon electron transfer-based bioorthogonal cleavage reaction for precision tumor therapy, *Adv. Mater.*, 2025, 2418134.

25 S. Yu, H. Kang, S. Jee, W. Moon, D. Jang, W.-T. Huang, D. Kim, K. Chung, D.-I. Won, J. Park, R.-S. Liu, K. Choi, S. Kim, L. P. Lee and D. H. Kim, MOF-based single-atom and metal cluster catalysts by room-temperature synthesis for tumor therapy, *Adv. Healthcare Mater.*, 2025, 2501058.

26 H. Kang, S. Yu, R. M. Kim, Y. Kim, S. C. Shin, D. Jang, J. H. Han, S. Hong, E. E. Kim, S. H. Kim, D. J. Ahn, J. W. Han, S. Kim, K. T. Nam, L. P. Lee and D. H. Kim, Optically tunable catalytic cancer therapy using enzyme-like chiral plasmonic nanoparticles, *Nat. Commun.*, 2025, **16**, 2562.

27 Y. Tian and T. Tatsuma, Plasmon-induced photoelectrochemistry at metal nanoparticles supported on nanoporous TiO_2, *Chem. Commun.*, 2004, 1810–1811.

28 Y. Li, M. B. Majewski, S. M. Islam, S. Hao, A. A. Murthy, J. G. DiStefano, E. D. Hanson, Y. Xu, C. Wolverton, M. G. Kanatzidis, M. R. Wasielewski, X. Chen and V. P. Dravid, Morphological engineering of winged $Au@MoS_2$ heterostructures for electrocatalytic hydrogen evolution, *Nano Lett.*, 2018, **18**, 7104–7110.

29 R. Bar-Ziv, P. Ranjan, A. Lavie, A. Jain, S. Garai, A. B. Hen, R. Popovitz-Biro, R. Tenne, R. Arenal, A. Ramasubramaniam, L. Lajaunie and M. Bar-Sadan, $Au-MoS_2$ hybrids as hydrogen evolution electrocatalysts, *ACS Appl. Energy Mater.*, 2019, **2**, 6043–6050.

30 J.-E. Lee, F. Marques Mota, C. H. Choi, Y.-R. Lu, R. Boppella, C.-L. Dong, R.-S. Liu and D. H. Kim, Plasmon-enhanced electrocatalytic properties of rationally designed hybrid

nanostructures at a catalytic interface, *Adv. Mater. Interfaces*, 2018, **5**, 1801144.

31 W. Zhang, J. Li, X.-H. Xia and Y.-G. Zhou, Enhanced electrochemistry of single plasmonic nanoparticles, *Angew. Chem., Int. Ed.*, 2022, **61**, 202115819.

32 R. T. P. da Silva, *et al.*, AgAu hollow nanoshells on graphene oxide as plasmonic nanozymes, *ACS Appl. Nano Mater.*, 2021, **4**, 12062–12072.

33 W. Jiang, D. Sun, C. Cai and H. Zhang, Sensitive detection of extracellular hydrogen peroxide using plasmon-enhanced electrochemical activity on Pd-tipped Au nanobipyramids, *Analyst*, 2023, **148**, 3791–3807.

34 S. K. Maji, Plasmon-enhanced electrochemical biosensing of hydrogen peroxide from cancer cells by gold nanorods, *ACS Appl. Nano Mater.*, 2019, **2**, 7162–7169.

35 D. Datta, J. W. Lim, R. C. Maji and S. K. Maji, Graphene oxide-wrapped gold nanorods for direct plasmon-enhanced electrocatalysis to detect hydrogen peroxide and in the hydrogen evolution reaction, *ACS Appl. Nano Mater.*, 2023, **6**, 2729–2740.

36 Q. Li, X. Zhuo and S. Li, *et al.*, Production of monodisperse gold nanobipyramids with number percentages approaching 100% and evaluation of their plasmonic properties, *Adv. Opt. Mater.*, 2015, **3**, 801–812.

37 S.-C. Chou, M. De, J. Kim, S. Byun, C. Dykstra, J. Yu, J. Huang and V. P. David, Ligand conjugation of chemically exfoliated MoS₂, *J. Am. Chem. Soc.*, 2013, **135**, 4584–4587.

38 P. B. Johnson and R. W. Christy, Optical constants of the noble metals, *Phys. Rev. B*, 1972, **6**, 4370–4379.

39 A. R. Beal and H. P. Hughes, Kramers-Kronig analysis of the reflectivity spectra of 2H-MoS₂, 2H-MoSe₂ and 2H-MoTe₂, *J. Phys. C*, 1979, **12**, 881–891.

40 S. Majumder, B. Satpati, S. Kumar and S. Banerjee, Multi-functional reduced graphene oxide wrapped circular Au nanoplatelets: enhanced photoluminescence, excellent surface-enhanced Raman scattering, photocatalytic water splitting, and non-enzymatic biosensor, *ACS Appl. Nano Mater.*, 2018, **1**, 3945–3955.

41 M. Gerlache, Z. Senturk, G. Quarin and J. M. Kauffmann, Electrochemical behavior of H₂O₂ on gold, *Electroanalysis*, 1997, **9**, 1088–1092.

42 D. Guziejewski, L. Stojanov, R. Gulaboski and V. Mirceski, Reversible and quasireversible electron transfer under conditions of differential square-wave voltammetry, *J. Phys. Chem. C*, 2022, **126**, 5584–5591.

43 D. Yin, X. Bo, J. Liu and L. Guo, A novel enzyme-free glucose and H₂O₂ sensor based on 3D graphene aerogels decorated with Ni₃N nanoparticles, *Anal. Chim. Acta*, 2018, **1038**, 11–20.

44 S.-S. Wang, W.-C. Hu, F.-F. Liu and C. Wang, Insights into direct plasmon-activated electrocatalysis on gold nanostar *via* efficient photothermal effect and reduced activation energy, *Electrochim. Acta*, 2019, **301**, 359–365.

45 C. Wang, X.-G. Nie, Y. Shi, Y. Zhou, J.-J. Xu, X.-H. Xia and H.-Y. Chen, Direct plasmon-accelerated electrochemical reaction on gold nanoparticles, *ACS Nano*, 2017, **11**, 5897–5905.

46 L. Cao, P. Wang, L. Chen, Y. Wu and J. Di, A photoelectrochemical glucose sensor based on gold nanoparticles as a mimic enzyme of glucose oxidase, *RSC Adv.*, 2019, **9**, 15307–15313.

47 S. K. Maji, S. Khan and R. Mondal, Plasmon-accelerated electrocatalysis based on gold nanostructures for electrochemical reactions and biosensing applications: a review, *ACS Appl. Nano Mater.*, 2024, **7**, 13821–13835.

48 X. Sun, S. Guo, Y. Liu and S. Sun, Dumbbell-like PtPd–Fe₃O₄ nanoparticles for enhanced electrochemical detection of H₂O₂, *Nano Lett.*, 2012, **12**, 4859–4863.

49 B. Dou, J. Yang, R. Yuan and Y. Xiang, Trimetallic hybrid nanoflower-decorated MoS₂ nanosheet sensor for direct in situ monitoring of H₂O₂ secreted from live cancer cells, *Anal. Chem.*, 2018, **90**, 5945–5950.

50 J. J. Q. Gonzalez, A. J. Medina-Olivera, R. Manzorro, C. Pardanaud, A. B. Hungria, L. Cubillana-Aguilera, J. M. Palacios-Santander, J. C. H. Garrido and L. Lajaunie, Defects engineering of Au@MoS₂ nanostructures for conventional and plasmon-enhanced hydrogen evolution reaction, *Int. J. Hydrogen Energy*, 2024, **51**, 371–382.

51 P. Zhang, M. Fujitsuka and T. Majima, Hot electron-driven hydrogen evolution using anisotropic gold nanostructure assembled monolayer MoS₂, *Nanoscale*, 2017, **9**, 1520–1526.

52 E. P. C. Higgins, A. A. Papaderakis, C. Byrne, R. Cai, A. Elgendy, S. J. Haigh, A. S. Walton, D. L. Lewis and R. A. W. Dryfe, High-performance nanostructured MoS₂ electrodes with spontaneous ultralow gold loading for hydrogen evolution, *J. Phys. Chem. C*, 2021, **125**, 20940–20951.

53 Y. Kang, Y. Gong, Z. Hu, Z. Li, Z. Qiu, Z. Zhu, P. M. Ajayan and Z. Fang, Plasmonic hot electron enhanced MoS₂ photocatalysis in hydrogen evolution, *Nanoscale*, 2015, **7**, 4482–4488.

54 L. Yao, J. Guo, C. Yang, Z. Li, S. Sun, M. Yue, W. Zuo, X. Zhang, H. Wang, F. A. Ibrahim, M. S. Hamdy, W. Lu, X. Sun and B. Tang, A synergistic strategy of Fe doping and anion protection enables efficient and robust seawater electrolysis, *Chem. Commun.*, 2025, **61**, 12377–12380.

55 L. Yao, J. Yang, Z. Li, Z. Cai, C. Yang, S. Sun, M. Yue, M. Zhang, X. Wang, H. Wang, Y. Luo, F. Sun, W. Lu, X. Sun and B. Tang, *Inorg. Chem.*, 2025, **64**, 2458–2467.